



Cite this: *Soft Matter*, 2025, 21, 4288

## Pattern formation of lipid domains in bilayer membranes†

Qiwei Yu <sup>a</sup> and Andrej Košmrlj <sup>\*bc</sup>

Phase separation plays an important role in spatial organization and material distribution of biological membranes, which are essential for crucial biological functions ranging from signaling and stress response to vesicle trafficking. Domains arising from demixing of molecules coarsen indefinitely unless growth is arrested at a finite size by additional mechanisms (e.g., membrane elasticity). The resulting finite-size domains self-organize into regular patterns such as stripes and dots, which are called modulated phases. Here, we examine the size and morphology of lipid domains with a minimal theoretical model that considers both the elastic deformation of the membrane and the chemical interactions between lipids, which are coupled by a preferred membrane curvature that depends on the local lipid composition. Microscopically, the coupling is caused by an asymmetry between leaflets which emerges after extra lipids (e.g., DPPC) are introduced to the outer leaflet. The additional lipid partitions preferentially to domains where it is enriched, creating a preferred curvature that depends on local composition. We use an amplitude expansion to determine the domain size and morphology of patterns that minimize the total free energy, which is validated by numerical simulations and compared against experiments in synthetic model membranes and cell-derived membranes. The morphology of patterns varies with membrane lipid composition following a complex morphological diagram, which is in good agreement with experiments. The domain size decreases monotonically with a membrane bending modulus but can be non-monotonic with surface tension. Our results offer testable predictions, such as pattern hysteresis upon cycling external stimuli, diverse pattern morphology near critical points, and non-monotonic dependence of the domain size on osmotic pressure, which motivate future experiments. The presented theoretical framework is generally applicable to pattern formation on deformable surfaces.

Received 14th March 2025,  
Accepted 3rd May 2025

DOI: 10.1039/d5sm00276a

[rsc.li/soft-matter-journal](http://rsc.li/soft-matter-journal)

## 1 Introduction

The heterogeneous spatial organization of lipids, proteins, and other components of biological membranes plays a crucial role in essential physiological functions.<sup>1,2</sup> To understand the mechanism underpinning the formation of these spatial structures, several model systems have been established, including cell-derived membranes<sup>3</sup> and artificial membrane systems such as giant unilamellar vesicles (GUVs).<sup>4,5</sup> One important mechanism is liquid–liquid phase separation, which organizes the membrane into domains with distinct compositions. These phase-separated domains participate in the regulation of various physiological processes, such as signaling, immune response, and vesicle trafficking.<sup>6–10</sup> Notably, phase separation in yeast vacuoles can

promote survival under stress by organizing proteins for a nutrient-sensing pathway or by facilitating lipophagy.<sup>11–13</sup> One possible mechanism for lipid domains to achieve regulatory functions is by facilitating condensation of proteins on the membrane through a prewetting transition.<sup>14</sup>

One important aspect of membrane organization is how domain size and morphology are regulated. In artificial membranes, phase separation has been observed in membranes consisting of as few as three components.<sup>4,15,16</sup> When the membrane is quenched into the 2-phase region, phase separation commences with the nucleation of many small droplets, which subsequently grow in size until reaching the dimension of the system.<sup>17</sup> Eventually, only a few macroscopic domains persist. Under certain conditions (such as bilayer asymmetry), however, the domains can remain at a small size and form stable periodic patterns such as stripes or dots. These extensive periodic structures are also referred to as “modulated phases”.<sup>18–21</sup> These domains do not strictly result from equilibrium phase separation, where only one domain of each phase should remain; however, we use the term “phase separation” to reflect that lipid demixing arises from the same interactions as macroscopic phase separation, in line with

<sup>a</sup> Lewis-Sigler Institute for Integrative Genomics, Princeton University, Princeton, NJ 08544, USA

<sup>b</sup> Department of Mechanical and Aerospace Engineering, Princeton University, Princeton, NJ 08544, USA. E-mail: [andrej@princeton.edu](mailto:andrej@princeton.edu)

<sup>c</sup> Princeton Materials Institute, Princeton University, Princeton, NJ 08544, USA

† Electronic supplementary information (ESI) available. See DOI: <https://doi.org/10.1039/d5sm00276a>



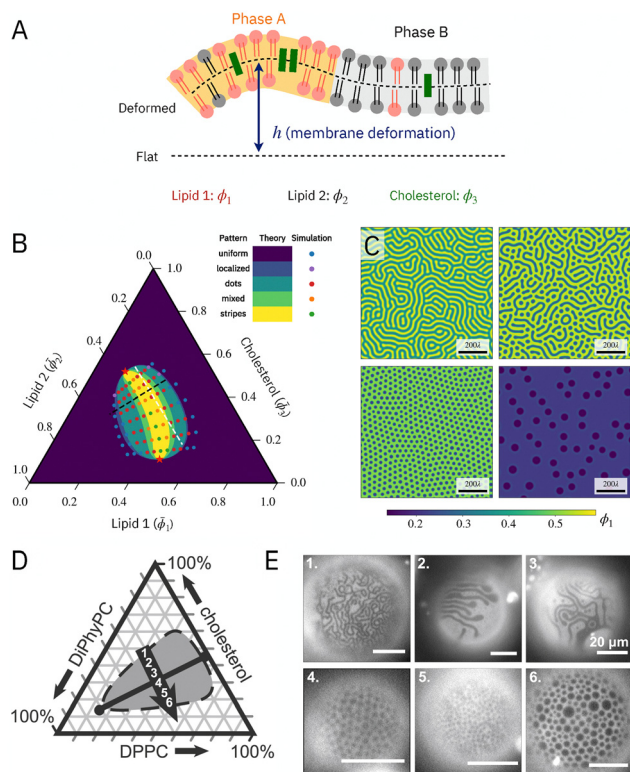


**Fig. 1** The theoretical model captures pattern formation on the membrane. (A) Schematics of the model. The membrane consists of three molecules: the two phospholipids (pink and gray) and cholesterol (green). They demix into phase A (yellow) and phase B (gray). Phase A is rich in lipid species 1 and therefore more curved.  $h$  describes the deformation of the membrane. (B) Pattern morphology as a function of the average volume fractions  $\bar{\phi}_{1,2,3}$ . The colored regions indicate analytical predictions of the morphology, and the colored dots are numerical simulations. The black dashed line indicates a typical tie line, with the white line indicating its perpendicular direction. The two critical points are marked by red  $\star$ . (C) Examples of the steady-state solution  $\phi_1(x,y)$  with different pattern morphologies, including stripes [upper left,  $(\bar{\phi}_1, \bar{\phi}_2) = (0.45, 0.40)$ ], mixed [upper right,  $(\bar{\phi}_1, \bar{\phi}_2) = (0.45, 0.34)$ ], and localized [lower left,  $(\bar{\phi}_1, \bar{\phi}_2) = (0.43, 0.29)$ ], and localized [lower right,  $(\bar{\phi}_1, \bar{\phi}_2) = (0.21, 0.25)$ ] patterns. (D) and (E) Experimental phase diagram and micrographs for DiPhyPC/DPPC/cholesterol vesicles, reproduced from Fig. 10 of Cornell *et al.*<sup>18</sup> with permission. The black line connecting the circles denotes a tie line. Parameters for (B) and (C):  $\chi_{12} = 1.8$ ,  $\chi_{13} = 1.4$ ,  $\chi_{23} = 1.65$ ,  $\xi = 4.8$ ,  $\kappa = 20$ ,  $\sigma = 0.1$ ,  $c_1 = 1/\sqrt{20} = 0.22$ .

terminology in the field.<sup>22,23</sup> A recent experiment<sup>18</sup> studied in detail domains in both synthetic membranes (GUVs) and cell-derived membranes by measuring their length scale and spatial organization under different experimental conditions, including temperature, membrane composition, and tension (see Fig. 1E for micrographs of patterns). The domain size was found to increase with surface tension but decrease with temperature, and the morphology could switch between stripes and dots as the average lipid composition was varied (see Fig. 1D and E). These quantitative measurements enabled close comparisons with multiple existing theories.<sup>20–38</sup> In particular, two of the approaches considered spontaneous curvature at the level of monolayer<sup>25,26</sup> and bilayer.<sup>22</sup> Both captured many aspects of the experiments, but neither appeared consistent with all the observations:<sup>18</sup> the

monolayer theory incorrectly predicts anti-registration between leaflets; the bilayer theory does not capture the morphology near the critical points, possibly because it employed a simplified depiction of the free energy of chemical interactions of lipids, which only contained a line tension between different domains. Other mechanisms were also considered but ruled out, including correlated critical fluctuations<sup>30</sup> or lipid cycling.<sup>34</sup> Electric dipole interaction can drive pattern formation in lipid monolayers,<sup>39–41</sup> but it does not appear to be the dominant mechanism for domain formation in a bilayer.<sup>18,27–29</sup> Lineactants effects are also unlikely since the system lacks hybrid lipids,<sup>18,31</sup> and the additional DPPC would likely partition to one of the domains instead of at the interface.<sup>42,43</sup> Thus, finding a theory consistent with the existing measurements will be crucial for understanding the mechanism underlying lipid domain formation.

In this work, we present a minimal theoretical model to demonstrate that local curvature-composition coupling is sufficient for explaining existing experiments. Specifically, the model incorporates both the elastic deformation of the membrane and the chemical interactions of lipids, which are coupled by a preferred membrane curvature. The preferred curvature depends on the composition of lipids and emerges from a leaflet asymmetry resulting from introducing extra lipids to the outer leaflet, which was indeed an essential procedure for stabilizing small domains in the experiments.<sup>18</sup> Our model demonstrates that the coupling between curvature and composition arrests the coarsening of lipid domains, leading to patterns at a finite length scale. This model shares ingredients of previous works on curvature-composition coupling,<sup>22,24–26,35</sup> but we aim to identify the minimal model to explain the experimentally observed patterns.

Our model generates useful insights into pattern size and morphology. First, we use an amplitude expansion to obtain analytical solutions for all possible patterns, which are confirmed by numerical simulations of the full model. In particular, we construct a phase diagram of all possible morphologies in a ternary membrane, providing important intuitions for systematically probing them in experiments. Second, the theory also predicts that domain size decreases with temperature and increases with membrane tension when the tension is sufficiently large, consistent with experiments. Third, amplitude expansion identifies bistability between morphologies and predicts that the morphology will undergo hysteresis when parameters such as osmotic pressure or temperature are cycled. The hysteresis is demonstrated in the simulations and can be tested in experiments in order to further constrain model parameters. It will also be interesting to study the dynamics of defects during morphological transitions. Overall, these results uncover new directions for probing the mechanism underlying small domains in biological membranes and provide valuable insights for understanding pattern formation on curved and deformable surfaces.

## 2 Model and methods

The theory considers three interacting lipid species that can move on a deformable bilayer membrane (Fig. 1A). They include



two phospholipids (red and gray) (such as DPPC and DiPhyPC used in ref. 18) and cholesterol (green). The shape of the membrane is described by the height field  $h(\vec{r})$ , defined as the distance from a flat reference plane. The composition of the membrane is defined by the (local) volume fractions occupied by different molecules  $\phi_i(\vec{r})$ , with  $i = 1, 2, 3$  labeling the three lipid species, respectively. They are constrained by an incompressibility condition  $\sum_{i=1}^3 \phi_i(\vec{r}) = 1$ . Motivated by experimental evidence,<sup>18</sup> the two leaflets of the bilayer are assumed to be in registration, *i.e.* with the same volume fractions. Therefore, only a single set of fields  $\phi_i(\vec{r})$  is considered for both leaflets. The membrane composition and shape undergo dynamics governed by the following free energy:

$$\mathcal{F}[h, \phi_1, \phi_2] = \int d^2\vec{r} [f_e(h, \phi_1, \phi_2) + f_c(\phi_1, \phi_2)], \quad (1)$$

where  $f_e$  and  $f_c$  are the free energy densities for the elastic deformation of the membrane and the chemical interactions between lipids (which include both the interaction energy and the mixing entropy of lipids), respectively. Here, we take the small slope approximation ( $|\nabla h| \ll 1$ ) so that all the fields can be defined on the flat reference plane [ $\vec{r} = (x, y)$ ]. The free energy due to membrane deformation is given by

$$f_e(h, \phi_1, \phi_2) = \frac{\kappa}{2} (\nabla^2 h - c_1 \phi_1)^2 + \frac{\sigma}{2} (\nabla h)^2, \quad (2)$$

where  $\kappa$  and  $\sigma$  are the bending rigidity and surface tension of the membrane, respectively.  $c_1$  is the preferred bilayer curvature induced by lipid species 1. This term is related to the bilayer asymmetry introduced in the experiments.<sup>18</sup> For a single leaflet, preferred curvature can arise from the non-cylindrical shapes of the lipid molecules. For a symmetric bilayer, however, opposite curvatures are induced in the two leaflets, which completely cancel out unless there is an asymmetry between the two leaflets. Indeed, the observed patterns of small domains only emerged after extra lipids (DPPC) were introduced to the outer leaflet,<sup>18</sup> which creates an asymmetry between the two leaflets and enables a non-zero preferred bilayer curvature. The microscopic picture is that the additional DPPC preferentially partitions to the domain in which it is enriched (Fig. 1A), thereby enhancing the preferred curvature in the outer leaflet and creating a net bilayer curvature preference. The magnitude of this effect  $c_1$  is related to the amount of asymmetry introduced to the bilayer, which can be controlled by the type and amount of lipids added to the outer leaflet. The local curvature depends on the local lipid enrichment, which we keep to the linear order in  $\phi_1$ . Although all lipid species can, in principle, induce preferred curvature, we only consider lipid species 1 both for simplicity and for consistency with experiments<sup>18</sup> where bilayer asymmetry is only introduced in the DPPC composition. Generalization to multiple curvature-generating lipids is straightforward by replacing  $c_1 \phi_1$  with  $\sum_i c_i \phi_i$ .

The second part of the free energy comes from the interaction and mixing of lipids:

$$f_c(\phi_1, \phi_2) = nk_B T \left[ \sum_{i=1}^3 \phi_i \ln \phi_i + \frac{1}{2} \sum_{i,j=1}^3 \chi_{ij} (\phi_i \phi_j - \lambda^2 \nabla \phi_i \cdot \nabla \phi_j) + \xi \phi_1 \phi_2 \phi_3 \right], \quad (3)$$

where  $\phi_3 = 1 - \phi_1 - \phi_2$ . The free energy is an extension of the Flory–Huggins model for regular solutions,<sup>44,45</sup> with  $n$  being the number density of the lipids,  $k_B$  the Boltzmann constant, and  $T$  the ambient temperature.  $\chi_{ij}$  is the two-body interaction parameter between  $\phi_i$  and  $\phi_j$  with interaction range  $\lambda$ . The term containing gradients  $\nabla \phi_i$  describes the interfacial properties with characteristic interface width given by  $\lambda$ .  $\xi$  characterizes the three-body interaction, which was shown to be important for the closed-loop miscibility gap<sup>46</sup> reported for these membranes,<sup>18,47</sup> where the presence of all three components is required for phase separation to occur. A model with a similar mathematical form (albeit with a different interpretation of leaflet registration) has been studied,<sup>35</sup> but it used a simpler description of lipids interactions, which restricted the possible non-uniform states to only stripes.

The free energy governs the time evolution of the fields, with  $h$  undergoing unconserved (model A) dynamics and  $\phi_{1,2}$  undergoing conserved (model B) dynamics:<sup>48</sup>

$$\frac{\partial h}{\partial t} = -M_h \frac{\partial \mathcal{F}}{\partial h}, \quad \frac{\partial \phi_i}{\partial t} = M_i \nabla^2 \frac{\partial \mathcal{F}}{\partial \phi_i} \quad (i = 1, 2), \quad (4)$$

where  $M_h$  and  $M_i$  are the mobilities of  $h$  and  $\phi_i$ , respectively.  $\phi_3 = 1 - \phi_1 - \phi_2$  is fully determined by  $\phi_1$  and  $\phi_2$ , and its dynamics is not considered explicitly. We measure energy in units of  $nk_B T$  and consider the nondimensionalized free energy density due to chemical interactions  $\tilde{f}_c = f_c/(nk_B T)$  as well as the nondimensionalized material properties  $\tilde{\kappa} = \kappa/(nk_B T)$ ,  $\tilde{\sigma} = \sigma \lambda^2/(nk_B T)$ . Space is rescaled as  $\tilde{x} = x/\lambda$ , and the preferred curvature is rescaled as  $\tilde{c}_1 = \lambda c_1$ . For the sake of simplicity, we assume equal mobilities  $M_1 = M_2 = M$  and rescale time as  $\tilde{t} = t/t_0 = tnk_B TM/\lambda^2$  so that the rescaled mobilities are 1.  $h$  is nondimensionalized so that the rescaled  $M_h$  is also 1. From now on, we will omit  $\tilde{\phantom{x}}$  and refer to nondimensionalized quantities unless explicitly stated.

In this theory, the preferred curvature plays the key role of coupling deformation  $h$  and concentrations  $\phi_i$ . In the absence of preferred curvature ( $c_1 = 0$ ), the membrane is flat ( $h = 0$ ) and the concentrations behave like a typical ternary liquid mixture, which is either uniform or demixed into different domains. When demixed, the domains coarsen perpetually until they reach the system size. These large domains have been observed in many membrane systems.<sup>16,17,49</sup> By coupling the concentrations to membrane deformation, the preferred curvature introduces an effective free energy cost against coarsening, which, when significant enough, arrests domain coarsening at a finite length scale. Hence, as will be shown analytically in the following sections, the steady-state domain size is selected by a competition between the chemical interactions of lipids and



membrane deformation. This mechanism should be distinguished from that of domain formation in block copolymers, where the energetic repulsion between constituent monomers is balanced by the entropic forces of polymer chain configurations.<sup>50–55</sup> The latter is usually referred to as microphase separation, which is fundamentally different from the mechanism described here.

Numerical simulation of the model reveals patterns with a variety of morphologies (Fig. 1C), including stripes, dots (arranged in a hexagonal lattice), mixed states (a combination of stripes and dots), and localized states (isolated and stationary droplets). These patterns are similar to those observed in experiments<sup>18</sup> and are reminiscent of those found in phase field crystal models.<sup>56–62</sup> The stable morphology of the pattern depends on the average composition of the membrane  $\bar{\phi}_i$ , which is illustrated by a phase diagram (Fig. 1B). The parameters were chosen such that the phase diagram qualitatively resembles that measured experimentally (Fig. 1D and E).<sup>18</sup> The same set of parameters is used throughout unless varied explicitly. Note that each of the morphologies is a modulated phase of macroscopic extent, each of which occupies a distinct region in the phase diagram (Fig. 1B). Here, we refer to them as “states” to avoid confusion with individual lipid domains that arise from demixing, which may experience coarsening arrest to form finite domains. In the following, we characterize these patterns combining analytical and numerical methods and discuss implications for both existing and future experiments.

## 3 Results

### 3.1 Membrane deformation arrests domain coarsening

We start by analyzing the size of the small domains. The characteristic domain size is defined as

$$L_c(t) \equiv 2\pi \sqrt{\int |\phi_1(\vec{k})|^2 d^2\vec{k}} / \sqrt{\int |\phi_1(\vec{k})|^2 k^2 d^2\vec{k}},$$

where  $\phi_i(\vec{k}) = \int \phi_i(\vec{r}) e^{-i\vec{k}\cdot\vec{r}} d^2\vec{r}$  is the Fourier transform of the concentration field. Fig. 2A and B shows the time evolution of domain size  $L_c(t)$  for different bending modulus  $\kappa$  and membrane tension  $\sigma$ . In the limit of small  $\kappa$  and large  $\sigma$ , the system behaves like a typical ternary mixture, with domain coarsening following the standard  $L_c(t) \propto t^{1/3}$  scaling (black triangles). This scaling is consistent with coarsening by either (Brownian-motion induced) coalescence or Ostwald ripening,<sup>63,64</sup> and has been reported in taut membranes.<sup>17</sup> For large  $\kappa$  and small  $\sigma$ , however, domain coarsening is arrested at a finite length scale, which sets the size of the patterns.

The finite droplet size is selected by a competition between the energy costs of membrane deformation and phase separation, with the former preferring small-scale variations and the latter large domains. The deformation energy depends on the height field  $h(\vec{r})$ , whose steady-state solution can be given in the Fourier space:

$$h(\vec{k}) = -\frac{\kappa c_1}{(\kappa k^2 + \sigma)} \delta\phi_1(\vec{k}), \quad (5)$$

where  $k = |\vec{k}|$  and  $\delta\phi_1(\vec{k})$  is the Fourier transform of  $\delta\phi_1(\vec{r}) = \phi_1(\vec{r}) - \bar{\phi}_1$  with  $\bar{\phi}_1$  being the mean concentration of lipid species 1.

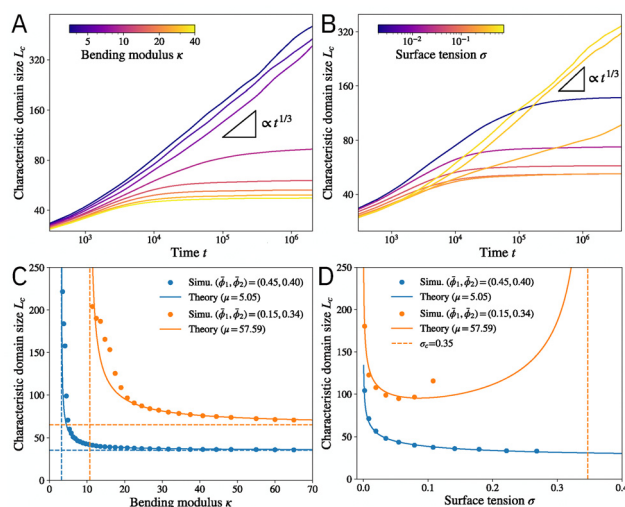


Fig. 2 (A) and (B) The time evolution of the characteristic domain size  $L_c$  for different (A) bending modulus  $\kappa$  and (B) membrane tension  $\sigma$ . The black triangles indicate  $t^{1/3}$  scaling. Mean composition:  $(\bar{\phi}_1, \bar{\phi}_2) = (0.38, 0.36)$ . (C) The characteristic domain size  $L_c$  as a function of the bending modulus  $\kappa$ . The solid lines indicate theory [eqn (9)] with the fitted value of the line tension  $\mu$  between phases. The horizontal dashed lines are the limit of infinite bending modulus  $\kappa \rightarrow \infty$ , and the vertical dashed lines show the critical value  $\kappa_c = \sqrt{\sigma\mu}/c_1$  below which the characteristic domain size becomes unbounded. (D) The characteristic domain size  $L_c$  as a function of the membrane tension  $\sigma$ . The vertical dashed line shows  $\sigma_c = \kappa^2 c_1^2 / \mu$  beyond which the characteristic domain size becomes unbounded. For the blue curve,  $\sigma_c$  is outside the range of the plot. Parameters are the same as in Fig. 1 unless otherwise stated. All quantities are nondimensionalized as discussed in the text.

Therefore, the deformation field follows the concentration profile. It stays flat for the uniform state and gets modulated once patterns form (Fig. 1C). Using  $h$  from eqn (5) simplifies the steady-state free energy due to membrane deformation:

$$\mathcal{F}_e \equiv \int f_e(h, \phi_1, \phi_2) d^2\vec{r} = \frac{1}{2} \int \frac{\sigma \kappa c_1^2}{(\sigma + \kappa k^2)} |\delta\phi_1(\vec{k})|^2 \frac{d^2\vec{k}}{(2\pi)^2}. \quad (6)$$

The coefficient  $\frac{\sigma \kappa c_1^2}{(\sigma + \kappa k^2)}$  decreases monotonically with  $k$ , thereby favoring small length scales. However, it has to compete with the Flory–Huggins free energy  $\mathcal{F}_c \equiv \int f_c(\phi_1, \phi_2) d^2\vec{r}$ , which always favors large domains in order to reduce the interface length between domains. Since  $\mathcal{F}_e$  increases monotonically with  $\kappa$ , it dominates over  $\mathcal{F}_c$  when  $\kappa$  is large enough, resulting in finite domains. Conversely,  $\mathcal{F}_c$  dominates in the small  $\kappa$  limit, leading to  $t^{1/3}$  scaling as shown in Fig. 2A.

In the absence of membrane deformation energy ( $f_e$ ), phase separation occurs along tie lines of the ternary mixture phase diagram (determined by  $f_c$ ), which can be located by constructing the convex hull of the free energy landscape.<sup>65</sup> Motivated by numerical evidence, we assume that the full system ( $h \neq 0$ ) also demixes along the same tie lines, whose slope gives the ratio of the concentration change  $\delta\phi_2/\delta\phi_1$ , where  $\delta\phi_i = \phi_i - \bar{\phi}_i$  with  $\bar{\phi}_i$  being the average composition of component  $i$ . The assumption fixes the ratios of  $\delta\phi_i$  but not their magnitudes. Consequently,  $\mathcal{F}_c$  can be simplified by expanding along the tie line.



Combining it with  $\mathcal{F}_e$  leads to an effective total free energy (see ESI,† Section IB for derivation):

$$\mathcal{F}_{\text{eff}}[\delta\phi_1] = \sigma_{\text{eff}}A + \frac{1}{2} \int \left( \frac{\sigma\kappa c_1^2}{(\sigma + \kappa k^2)} + \mu k^2 \right) |\delta\phi_1(\vec{k})|^2 \frac{d^2\vec{k}}{(2\pi)^2} + \int \left[ -\frac{a}{2}\delta\phi_1(\vec{r})^2 + \frac{c}{3}\delta\phi_1(\vec{r})^3 + \frac{b}{4}\delta\phi_1(\vec{r})^4 \right] d^2\vec{r}, \quad (7)$$

where  $a, b, c$  are Ginzburg–Landau coefficients and  $\mu$  is related to the line tension between domains. They can be obtained by expanding the free energy along the tie lines.  $A$  is the total area of the membrane, with  $\sigma_{\text{eff}}$  being the effective surface energy density:

$$\sigma_{\text{eff}} = \sigma + f_c(\bar{\phi}_1, \bar{\phi}_2) + \frac{1}{2}\kappa c_1^2 \bar{\phi}_1^2. \quad (8)$$

The selection of the preferred length scale is dictated by the second term in the free energy eqn (7), which involves both a membrane deformation term that favors large  $k$  and a lipid interaction term that favors small  $k$ . Minimizing free energy with respect to  $k$  leads to the characteristic length scale (domain size)

$$L_c = \frac{2\pi}{k_c} = \frac{2\pi}{\sqrt{\frac{\sigma c_1^2}{\mu} - \frac{\sigma}{\kappa}}}, \quad (9)$$

with  $k_c$  being the characteristic wavevector. A similar form of  $k_c$  was found in ref. 35–38.

The predicted  $L_c$  is confirmed by numerical solution of the dynamical equations. Fig. 2C presents  $L_c$  as a function of the bending modulus  $\kappa$ . While small  $\kappa$  always leads to perpetual coarsening ( $L_c \rightarrow \infty$ ), coarsening is arrested beyond a critical value  $\kappa_c = \sqrt{\sigma\mu}/c_1$  (vertical dashed lines). The domain size  $L_c$  decreases monotonically with  $\kappa$  and converges to  $L_c = 2\pi(\sigma c_1^2/\mu)^{-1/4}$  in the infinite  $\kappa$  limit (horizontal dashed lines). The theory (solid lines) agrees well with numerical simulations (circles), with a single fitting parameter  $\mu$  to account for a modified line tension between the two phases since the chemical composition at the interface deviates slightly from the tie lines (Fig. S1, ESI†).  $\mu$  can also be estimated by expanding the free energy along the tie lines (see ESI,† Section IB), which leads to a slightly worse agreement (Fig. S2, ESI†).

The domain size  $L_c$  has a different functional dependence on the membrane tension  $\sigma$  (Fig. 2D). Finite domains only emerge when  $\sigma < \sigma_c = \kappa^2 c_1^2/\mu$ .  $L_c$  reaches minimum at an intermediate value  $\sigma_m = \kappa^2 c_1^2/(4\mu) = \sigma_c/4$  and diverges in limits  $\sigma \rightarrow 0$  and  $\sigma \rightarrow \sigma_c$ . In the  $\sigma \rightarrow 0$  limit, the energy cost for stretching is absent, so the preferred curvature condition can be satisfied everywhere on the membrane, allowing for indefinite coarsening. In addition to the divergence of domain size, another possibility in the large  $\sigma$  limit (taut membrane) is that the membrane remains flat inside each of the domains, and the system behaves like a ternary mixture with either a uniform concentration or coarsening droplets. The transition to the large  $\sigma$  regime is discussed below in a later section. As shown in Fig. 2D, the predicted  $L_c$  agrees well with numerical simulations. The membrane tension can be varied by

tuning the exterior osmotic pressure, which was found to monotonically increase domain size with tension for synthetic and cell-derived membranes.<sup>18</sup> These experiments are likely performed at relatively high membrane tension since the vesicles appeared taut before introducing DPPC to the outer leaflet. Moreover, large domains (in the sense that coarsening was not arrested) were observed toward the end of the experiment, indicating that  $\sigma$  eventually exceeds  $\sigma_c$ . Hence, they are consistent with the right branch ( $\sigma > \sigma_m$ ) of the predicted  $L_c(\sigma)$  (Fig. 2D). It will be interesting to measure the domain size at low membrane tension (which can be achieved by high exterior osmotic pressure) and look for potential non-monotonicity with tension.

Finally, we consider the effect of temperature  $T$ . While all the material properties and interaction parameters can depend on temperature, we assume that none of them varies drastically in the experimental range. Specifically, since energy is measured in units of  $nk_B T$ , the rescaled parameters  $\bar{\kappa}$ ,  $\bar{\sigma}$ ,  $\bar{\chi}$ , and  $\bar{\zeta}$  all have a  $1/(k_B T)$  dependence on temperature, while the entropy term does not. Since the two-phase region in the phase diagram shrinks with increasing temperature,<sup>47</sup> we expect the composition difference between the two domains and thus the line tension to decrease with temperature. Thus, the rescaled line tension  $\mu$  will likely decrease more rapidly than  $T^{-1}$ . Under this assumption, eqn (9) predicts that the characteristic domain size  $L_c$  decreases with temperature  $T$ , which is confirmed by numerical simulations (see Fig. S3, ESI†) and is consistent with experiments.<sup>18</sup>

### 3.2 Pattern morphology predicted by amplitude expansion

Next, we determine the steady-state pattern morphologies with an amplitude expansion around the uniform state:<sup>66</sup>

$$\delta\phi_1 = \phi_1 - \bar{\phi}_1 = \sum_n A_n e^{ik_n \vec{r}} + \text{c.c.}, \quad (10)$$

where  $A_n$  are the amplitudes of the Fourier modes and c.c. stands for the complex conjugate terms. For homogeneous patterns, it suffices to consider spatially uniform amplitudes. The time evolution of the amplitudes can be determined by substituting eqn (10) back to the equation of motion  $\frac{\partial \delta\phi_1}{\partial t} = \nabla^2 \frac{\partial \mathcal{F}_{\text{eff}}}{\partial \delta\phi_1}$  and keeping only the leading order terms in the amplitudes. This results in a dynamical system for  $\dot{A}_n(t) = F\{A_n(t)\}$ , whose fixed points correspond to different pattern morphologies. The stability of these fixed points determines possible steady-state patterns (see ESI,† Section I). Since the theory is an expansion in amplitudes, it is the most accurate near the critical points as the higher order terms in  $A_n$  become less important.

We find three fixed points representing uniform, dot (Fig. 1C, lower left), and stripe (Fig. 1C, upper left) morphologies, respectively. Their stability is governed by the following control parameter:

$$g = \frac{a_{\text{eff}} b}{c^2} \equiv \frac{b}{c^2} \left( a - 2\sqrt{c_1^2 \sigma \mu} + \frac{\mu \sigma}{\kappa} \right), \quad (11)$$

where  $a, b, c$  are Ginzburg–Landau coefficients defined in eqn (7) and eqn (S15)–(S17) in the ESI.† The uniform, dot, and stripe fixed



points are stable when  $g \in (-\infty, 0)$ ,  $\left(-\frac{1}{15}, \frac{16}{3}\right)$ , and  $\left(\frac{4}{3}, +\infty\right)$ , respectively. Stripes and dots are bistable in the overlap region  $g \in \left(\frac{4}{3}, \frac{16}{3}\right)$ ; their coexistence is referred to as the mixed state (Fig. 1C, upper right). In the coexistence region, the observed pattern is history-dependent. With random initialization, we find that dots and stripes form individual patches. The size of each dot or stripe domain is given by the characteristic length scale eqn (9), but the size of dot/stripe patches stabilizes at a finite value. The latter is likely due to kinetic trapping since rearranging dots and stripes requires going over a large free energy barrier. Another bistable region is  $g \in \left(-\frac{1}{15}, 0\right)$ , where individual dots are stable in a uniform background, which leads to localized states (Fig. 1C, lower right) similar to the localized states found in the Swift–Hohenberg equation.<sup>56,57</sup> The history dependence of morphologies in the bistable regions will be further illustrated by hysteresis (Fig. 4).

The predicted phase morphologies are summarized in a phase diagram (Fig. 1B), which are confirmed by numerical simulation (represented by filled circles). No fitting parameters are involved when constructing the phase diagram as  $(a, b, c, \mu)$  are evaluated by expanding the free energy along the tie lines. The agreement between theory and simulation is especially good near the two critical points (indicated by red stars), where the amplitude expansion is the most accurate. Moving away from the critical points, the expansion becomes less precise, but most of the morphologies are still correctly captured. The structure of the phase diagram is robust to the form of the interaction free energy of lipids  $f_c$ , as long as it exhibits generic phase separation behaviors.

The phase diagram is qualitatively consistent with experiments in GUVs.<sup>18</sup> In particular, when the mean composition is varied along any of the tie lines (a typical tie line is indicated by the black dashed line in Fig. 1B), the system always morphs from dots to stripes and eventually back to dots, which is the same as the sequence of morphologies observed in experiments<sup>18</sup> (Fig. 1D and E). When varied in the normal (perpendicular) direction (indicated by the white dashed line in Fig. 1B), the patterns can switch between dots and stripes, as observed in experiments.<sup>18</sup> The exact sequence of patterns is not unique: it depends on where the normal line crosses the tie line. Hence, further experimental characterization of the phase diagram of patterns formed after introducing extra lipids will be informative for determining the model parameters and understanding the underlying interactions.

The morphology near the critical points has been suggested as an important criterion for distinguishing different mechanisms for the small domains.<sup>18</sup> In particular, the observation of stripe domains near the critical point was used to rule out a previous model involving bilayer curvature.<sup>18,22</sup> In our model, however, the system can exhibit any of the morphologies near the two critical points (indicated by red stars), depending on the direction in which the critical point is approached. An analogous effect was reported in a diblock copolymer model,<sup>53</sup> although the physical mechanism for pattern formation is

different. Since all the phase boundaries become tangent to the miscibility boundary at the critical points, the stripe phase becomes dominant in its vicinity. In other words, if we draw a circle near the critical point  $(\phi_1^c, \phi_2^c)$  with radius  $\varepsilon$ , both the stripe phase and the uniform phase will occupy half the area in the circle as  $\varepsilon \rightarrow 0$ , with all the other morphologies occupying infinitesimal area. This may explain the experimental observation of stripes near the critical point. It will be interesting to test experimentally whether departing the critical point in different directions eventually leads to different morphologies.

### 3.3 Droplets coarsen in taut membranes

The small domains discussed so far only emerge at relatively low surface tension. As the membrane becomes more taut, its behavior approaches a ternary mixture with either a uniform state or large domains (in the sense that coarsening is not arrested). The transition into these two states are driven by different dynamical processes: the transition to the uniform state can be described by a saddle-node bifurcation in the amplitude space, while the transition to the large, coarsening domain phase is best understood as a crossover of free energy. Fig. 3 illustrates these two types of transitions. For transition to the uniform state, the morphology parameter  $g$  decreases with  $\sigma$  (in the regime where  $L_c$  stays finite) and eventually crosses the threshold  $g = -1/15$  (Fig. 3A), below which only the uniform state is stable. Throughout the transition, the deformation field

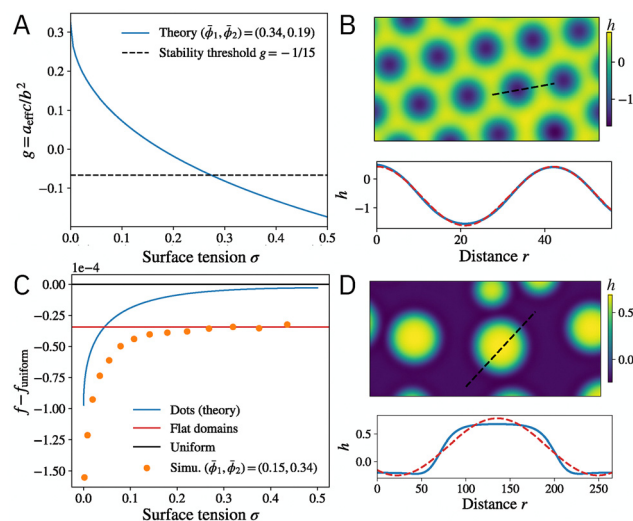


**Fig. 3** Domain coarsening in taut membranes. (A) The morphology control parameter  $g$  as a function of  $\sigma$ . The black dashed line is  $g = -1/15$  below which only the uniform solution is stable. (B) The deformation field  $h(\vec{r})$  across a droplet (blue line in the bottom panel, corresponding to the black dashed line in the top panel) can be well described by fitting  $h = h_0 + h_1 \sin(kr + \psi)$  (red dashed line). (C) The free energy density as a function of  $\sigma$ . Orange dots are simulation results; the blue line is calculated from amplitude expansion. The black and red lines are the free energy densities of the uniform state and flat droplet domains, respectively. (D)  $h(\vec{r})$  across a droplet. The deformation is flat except near the interface, which cannot be captured by fitting a shifted sin function (red dashed line). Mean composition: (A) and (B)  $(\bar{\phi}_1, \bar{\phi}_2) = (0.34, 0.19)$ ; (C) and (D)  $(\bar{\phi}_1, \bar{\phi}_2) = (0.15, 0.34)$ . Parameters are the same as Fig. 1 unless otherwise stated.



$h(\vec{r})$  can be well described by the sum of a few Fourier modes (eqn (10) and Fig. 3B), but its amplitude vanishes at large  $\sigma$  due to a saddle-node bifurcation. On the other hand, the transition to coarsening lipid domains can be understood by a free energy crossover. For these domains, the membrane remains flat ( $h = \text{const.}$ ) within bulk phases, which can no longer be described by the sum of Fourier modes (Fig. 3D). The composition of the bulk phases can be determined by a convex hull construction with an extra free energy penalty  $\frac{1}{2}\kappa c_1^2 \phi_1^2$  [see eqn (2)]. These flat droplets always coarsen to reach the system size. As shown in Fig. 3C, the free energy density of the patterns (blue line) increases with  $\sigma$  and eventually exceeds that of the flat droplet phase (red line). The crossover of free energy density defines a transition point beyond which patterns of finite-sized domains are no longer observed. This crossover is also observed in simulations (orange dots).

### 3.4 Hysteresis of pattern morphologies

The bistability of stripes and dots in the mixed state suggests the possibility for the hysteresis of pattern morphology due to cycling control parameters. Namely, it is possible to observe either or a mixture of these two morphologies depending on the history of the control parameter. One of the most accessible parameters is membrane tension, which can be tuned by exterior osmotic pressure. Fig. 4 shows a hypothetical experiment where the external salt concentration is first increased and then decreased. Increasing salt concentration decreases the surface tension, which leads to a transition from dots to stripes; decreasing concentration leads to the opposite transition. Indeed, the backward transition takes place around  $\sigma = 0.185$ , which is much larger than the threshold for the forward transition  $\sigma = 0.135$ . Hysteresis is also observed when cycling temperature (see Fig. S4, ESI<sup>†</sup>), although we had to again assume that temperature dependence predominantly enters through the mixing entropy. Since the morphology control parameter  $g$  [eqn (11)] is non-monotonic in  $\sigma$ , it may also be possible to observe hysteresis in stripe-dot-stripe transitions by tuning the exterior salt concentration. These

hysteresis experiments will help elucidate the validity of the bistable solutions found here, and the transition thresholds may be used to quantitatively determine parameters in our model.

One interesting aspect of the pattern morphologies is the persistence of defects: places where the parallel stripes order or the hexagonal dots order are locally violated. These defects were also seen in experiments.<sup>18</sup> Since patterns are mesoscopic, thermal noise at this scale is not strong enough to effectively remove defects during experimentally relevant timescales. Indeed, these defects are common in mesoscopic patterns.<sup>67,68</sup> However, cycling parameters appear effective in reducing defects (*e.g.*, compare the initial and final state at  $\sigma = 0.21$  in Fig. 4). It will be interesting to study these defects in more detail both experimentally and theoretically.

## 4 Discussion

In this paper, we have proposed a theoretical model to describe the patterns formed by small domains in biological membranes. The model is minimal in the sense that it successfully captures existing measurements of the pattern morphology and length scales by only requiring local coupling between the bilayer curvature and the local lipid composition. Several future experimental directions are proposed to reveal more information on the underlying mechanism. One possibility is to tune the membrane tension in a larger dynamical range and in cycles to search for a non-monotonic change in the domain size as well as hysteresis of pattern morphologies. Another direction is to examine the rich structures of the morphological phase diagram (Fig. 1B) by carefully exploring the composition space. In particular, the theory predicts that different patterns can be observed when approaching the critical point (Fig. 1B, red stars) from different directions, which has not been explored experimentally.

The microscopic picture for curvature-composition coupling is that the extra lipids (DPPC) introduced to the outer leaflet partitions preferentially to lipid domains, inducing different

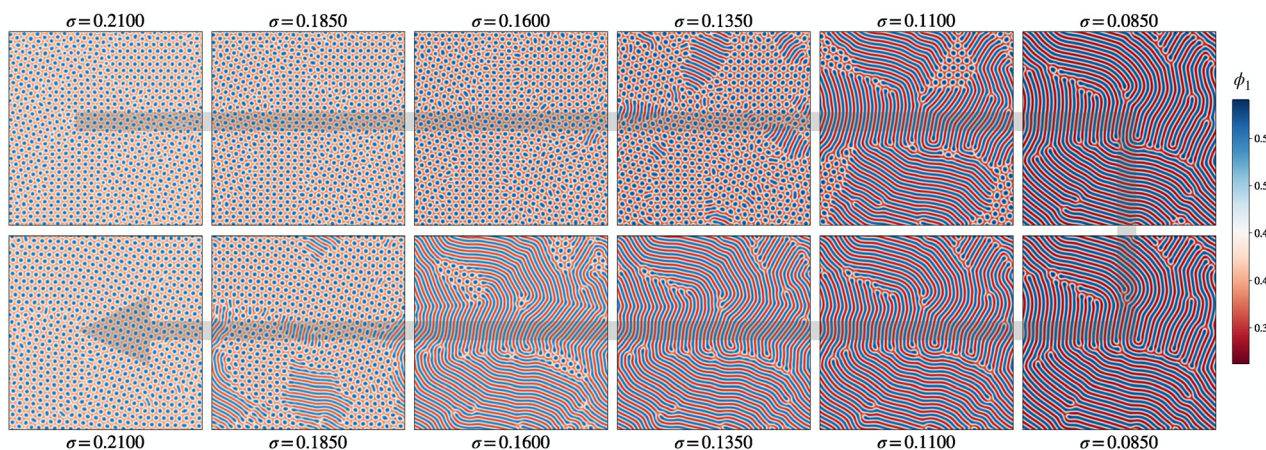


Fig. 4 Pattern hysteresis due to tuning the (non-dimensionalized) surface tension  $\sigma$ , which is first decreased and then increased (as indicated by the arrow), with a fixed composition  $(\phi_1, \phi_2) = (0.45, 0.40)$ . All the other parameters are the same as in Fig. 1.



local curvature. Hence, it will be interesting to test this hypothesis by exploring how the patterns depend on the amount of DPPC introduced to the outer leaflet, which affects the  $c_1$  parameter in the model. It should also be noted that while this particular mechanism should be tested, our results are valid for generic mechanisms for curvature-composition coupling, which will produce the same term to the first order in  $\phi_1$  but with a different interpretation of  $c_1$  that depends on the mechanism.

New experimental information will also enable further theoretical work, such as accurately fitting the phase boundaries and inverse design of pattern morphologies.<sup>69</sup> Another direction to extend the theory is to consider the hydrodynamics of the bulk solvent exhibiting either passive<sup>70</sup> or active flows<sup>71</sup> or by exploring the interactions between membrane proteins (especially ones that sense curvature<sup>72</sup>) and lipid domains in giant plasma membrane vesicles (GPMVs) and membranes of living cells.<sup>73,74</sup>

While we have mostly focused on lipid interactions, many important biological functions involve protein–membrane interactions.<sup>11–13,75–77</sup> For example, lipid domains could organize proteins in stress response.<sup>11–13</sup> They can also serve as substrates for proteins to phosphorylate/dephosphorylate.<sup>75</sup> Domains may form due to the phase separation of membrane proteins, such as cell adhesion receptors,<sup>76</sup> which form clustering patterns due to coupling with membrane deformation. Dot and stripe domains can also arise when phase-separating proteins bind to membranes and induce deformation.<sup>78</sup> The present formalism can be extended to include additional fields for membrane-associated proteins to describe these important biological processes. It will also be interesting to see if the model can be extended to include electric dipole interactions in order to study complex patterns observed in a monolayer at the air–water interface.<sup>39–41</sup>

The patterns discussed here arise from equilibrium interactions governed by an overall free energy. Nonetheless, biological membranes under physiological conditions are highly nonequilibrium, influenced by various active processes that physically deform<sup>79</sup> or chemically modify<sup>75,80</sup> the membrane. These nonequilibrium interactions enable rich spatiotemporal behaviors such as traveling waves of lipids,<sup>75</sup> proteins,<sup>81</sup> and membrane shape changes.<sup>82</sup> The clustering of lipids and proteins are important for biological functions such as cell shape regulation<sup>81,82</sup> and signaling.<sup>83–85</sup> By explicitly modeling the kinetics of nonequilibrium processes (e.g. phosphorylation/dephosphorylation cycles), the theoretical framework developed here can be extended to offer more insights into the morphology and dynamics of these nonequilibrium patterns.

## Author contributions

Q. Y. and A. K. designed research, performed research, and wrote the manuscript.

## Data availability

Details of the analytical derivations and numerical simulations have been included as part of the ESI.†

## Conflicts of interest

The authors declare no competing interests.

## Note added after first publication

This article replaces the version published on 5th May, which contained an error in the radius notation in Section 3.2.

## Acknowledgements

We thank S. L. Keller and I. Levin for introducing us to this experimental system and for many stimulating discussions at various stages of this work. We thank E. Frey, J. Dunkel, and M. Haataja for useful discussions. This work is supported by the National Science Foundation, through the Princeton Center for Complex Materials (DMR-2011750) and the Center for the Physics of Biological Function (PHY-1734030), and by the Princeton Catalysis Initiative. The work by Q. Y. is supported in part by a Harold W. Dodds Fellowship from Princeton University.

## References

- 1 S. Semrau and T. Schmidt, *Soft Matter*, 2009, **5**, 3174.
- 2 T. Sych, C. O. Gurdap, L. Wedemann and E. Sezgin, *Membranes*, 2021, **11**, 323.
- 3 T. Baumgart, A. T. Hammond, P. Sengupta, S. T. Hess, D. A. Holowka, B. A. Baird and W. W. Webb, *Proc. Natl. Acad. Sci. U. S. A.*, 2007, **104**, 3165–3170.
- 4 C. Dietrich, L. Bagatolli, Z. Volovyk, N. Thompson, M. Levi, K. Jacobson and E. Gratton, *Biophys. J.*, 2001, **80**, 1417–1428.
- 5 R. Dimova, S. Aranda, N. Bezlyepkina, V. Nikolov, K. A. Riske and R. Lipowsky, *J. Phys.: Condens. Matter*, 2006, **18**, S1151–S1176.
- 6 P. Sengupta, B. Baird and D. Holowka, *Semin. Cell Dev. Biol.*, 2007, **18**, 583–590.
- 7 P. S. Kabouridis, *Mol. Membr. Biol.*, 2006, **23**, 49–57.
- 8 S. Mañes and A. Viola, *Mol. Membr. Biol.*, 2006, **23**, 59–69.
- 9 R. G. Parton and A. A. Richards, *Traffic*, 2003, **4**, 724–738.
- 10 C. Salaün, D. J. James and L. H. Chamberlain, *Traffic*, 2004, **5**, 255–264.
- 11 A. Murley, J. Yamada, B. J. Niles, A. Toulmay, W. A. Prinz, T. Powers and J. Nunnari, *J. Cell Biol.*, 2017, **216**, 2679–2689.
- 12 A. Y. Seo, P.-W. Lau, D. Feliciano, P. Sengupta, M. A. L. Gros, B. Cinquin, C. A. Larabell and J. Lippincott-Schwartz, *eLife*, 2017, **6**, e21690.
- 13 C. L. Leveille, C. E. Cornell, A. J. Merz and S. L. Keller, *Proc. Natl. Acad. Sci. U. S. A.*, 2022, **119**, e2116007119.
- 14 M. Rouches, S. L. Veatch and B. B. Machta, *Proc. Natl. Acad. Sci. U. S. A.*, 2021, **118**, e2103401118.
- 15 S. L. Veatch and S. L. Keller, *Phys. Rev. Lett.*, 2002, **89**, 268101.
- 16 S. L. Veatch and S. L. Keller, *Biophys. J.*, 2003, **85**, 3074–3083.
- 17 C. Stanich, A. Honerkamp-Smith, G. Putzel, C. Warth, A. Lamprecht, P. Mandal, E. Mann, T.-A. Hua and S. Keller, *Biophys. J.*, 2013, **105**, 444–454.
- 18 C. E. Cornell, A. D. Skinkle, S. He, I. Levental, K. R. Levental and S. L. Keller, *Biophys. J.*, 2018, **115**, 690–701.



- 19 M. Seul and D. Andelman, *Science*, 1995, **267**, 476–483.
- 20 P. B. Sunil Kumar, G. Gompper and R. Lipowsky, *Phys. Rev. E: Stat. Phys., Plasmas, Fluids, Relat. Interdiscip. Top.*, 1999, **60**, 4610–4618.
- 21 R. Shlomovitz, L. Maibaum and M. Schick, *Biophys. J.*, 2014, **106**, 1979–1985.
- 22 J. Harden, F. MacKintosh and P. Olmsted, *Phys. Rev. E: Stat., Nonlinear, Soft Matter Phys.*, 2005, **72**, 011903.
- 23 T. R. Shaw, S. Ghosh and S. L. Veatch, *Annu. Rev. Phys. Chem.*, 2021, **72**, 51–72.
- 24 F. Schmid, *Biochim. Biophys. Acta, Biomembr.*, 2017, **1859**, 509–528.
- 25 M. Schick, *J. Phys. Chem. B*, 2018, **122**, 3251–3258.
- 26 D. W. Allender and M. Schick, *J. Membr. Biol.*, 2022, **255**, 451–460.
- 27 J. Liu, S. Qi, J. T. Groves and A. K. Chakraborty, *J. Phys. Chem. B*, 2005, **109**, 19960–19969.
- 28 J. Liu, J. T. Groves and A. K. Chakraborty, *J. Phys. Chem. B*, 2006, **110**, 8416–8421.
- 29 R. D. Usery, T. A. Enoki, S. P. Wickramasinghe, M. D. Weiner, W.-C. Tsai, M. B. Kim, S. Wang, T. L. Torng, D. G. Ackerman, F. A. Heberle, J. Katsaras and G. W. Feigenson, *Biophys. J.*, 2017, **112**, 1431–1443.
- 30 A. R. Honerkamp-Smith, B. B. Machta and S. L. Keller, *Phys. Rev. Lett.*, 2012, **108**, 265702.
- 31 Y. Hirose, S. Komura and D. Andelman, *Phys. Rev. E: Stat., Nonlinear, Soft Matter Phys.*, 2012, **86**, 021916.
- 32 S. Meinhardt, R. L. C. Vink and F. Schmid, *Proc. Natl. Acad. Sci. U. S. A.*, 2013, **110**, 4476–4481.
- 33 J. J. Amazon, S. L. Goh and G. W. Feigenson, *Phys. Rev. E: Stat., Nonlinear, Soft Matter Phys.*, 2013, **87**, 022708.
- 34 J. Fan, M. Sammalkorpi and M. Haataja, *Phys. Rev. Lett.*, 2010, **104**, 118101.
- 35 S. Sadeghi, M. Müller and R. Vink, *Biophys. J.*, 2014, **107**, 1591–1600.
- 36 F. C. MacKintosh, *Phys. Rev. E: Stat. Phys., Plasmas, Fluids, Relat. Interdiscip. Top.*, 1994, **50**, 2891–2897.
- 37 R. Shlomovitz and M. Schick, *Biophys. J.*, 2013, **105**, 1406–1413.
- 38 M. Schick, *Phys. Rev. E: Stat., Nonlinear, Soft Matter Phys.*, 2012, **85**, 031902.
- 39 H. M. McConnell, *Annu. Rev. Phys. Chem.*, 1991, **42**, 171–195.
- 40 S. L. Keller and H. M. McConnell, *Phys. Rev. Lett.*, 1999, **82**, 1602–1605.
- 41 D. J. Keller, H. M. McConnell and V. T. Moy, *J. Phys. Chem.*, 1986, **90**, 2311–2315.
- 42 B. Palmieri and S. A. Safran, *Langmuir*, 2013, **29**, 5246–5261.
- 43 C. J. Garvey, S. J. Bryant, A. Elbourne, T. Hunt, B. Kent, M. Kreuzer, M. Strobl, R. Steitz and G. Bryant, *J. Colloid Interface Sci.*, 2023, **638**, 719–732.
- 44 P. J. Flory, *J. Chem. Phys.*, 1942, **10**, 51–61.
- 45 M. L. Huggins, *J. Chem. Phys.*, 1941, **9**, 440.
- 46 T. Idema, J. M. J. van Leeuwen and C. Storm, *Phys. Rev. E: Stat., Nonlinear, Soft Matter Phys.*, 2009, **80**, 041924.
- 47 S. L. Veatch, K. Gawrisch and S. L. Keller, *Biophys. J.*, 2006, **90**, 4428–4436.
- 48 P. C. Hohenberg and B. I. Halperin, *Rev. Mod. Phys.*, 1977, **49**, 435–479.
- 49 M. Yanagisawa, M. Imai, T. Masui, S. Komura and T. Ohta, *Biophys. J.*, 2007, **92**, 115–125.
- 50 F. S. Bates and G. H. Fredrickson, *Annu. Rev. Phys. Chem.*, 1990, **41**, 525–557.
- 51 G. Fredrickson and F. Bates, *Annu. Rev. Mater. Sci.*, 1996, **26**, 501–550.
- 52 F. S. Bates and G. H. Fredrickson, *Phys. Today*, 1999, **52**, 32–38.
- 53 M. W. Matsen and M. Schick, *Phys. Rev. Lett.*, 1994, **72**, 2660–2663.
- 54 M. W. Matsen and F. S. Bates, *Macromolecules*, 1996, **29**, 1091–1098.
- 55 F. Liu and N. Goldenfeld, *Phys. Rev. A: At., Mol., Opt. Phys.*, 1989, **39**, 4805–4810.
- 56 U. Thiele, A. J. Archer, M. J. Robbins, H. Gomez and E. Knobloch, *Phys. Rev. E: Stat., Nonlinear, Soft Matter Phys.*, 2013, **87**, 042915.
- 57 E. Knobloch, *IMA J. Appl. Math.*, 2016, **81**, 457–487.
- 58 H. Emmerich, H. Löwen, R. Wittkowski, T. Gruhn, G. I. Tóth, G. Tegze and L. Gránágy, *Adv. Phys.*, 2012, **61**, 665–743.
- 59 K. R. Elder, Z.-F. Huang and N. Provatas, *Phys. Rev. E: Stat., Nonlinear, Soft Matter Phys.*, 2010, **81**, 011602.
- 60 P. Stefanovic, M. Haataja and N. Provatas, *Phys. Rev. Lett.*, 2006, **96**, 225504.
- 61 P. C. Matthews and S. M. Cox, *Nonlinearity*, 2000, **13**, 1293–1320.
- 62 S. M. Cox, *Phys. Lett. A*, 2004, **333**, 91–101.
- 63 I. Lifshitz and V. Slyozov, *J. Phys. Chem. Solids*, 1961, **19**, 35–50.
- 64 B. A. Camley and F. L. H. Brown, *J. Chem. Phys.*, 2011, **135**, 225106.
- 65 S. Mao, D. Kuldinow, M. P. Haataja and A. Košmrlj, *Soft Matter*, 2019, **15**, 1297–1311.
- 66 M. C. Cross and P. C. Hohenberg, *Rev. Mod. Phys.*, 1993, **65**, 851–1112.
- 67 N. Stoop and J. Dunkel, *Soft Matter*, 2018, **14**, 2329–2338.
- 68 D. Boyer and J. Viñals, *Phys. Rev. E: Stat., Nonlinear, Soft Matter Phys.*, 2002, **65**, 046119.
- 69 C. P. Goodrich, E. M. King, S. S. Schoenholz, E. D. Cubuk and M. P. Brenner, *Proc. Natl. Acad. Sci. U. S. A.*, 2021, **118**, e2024083118.
- 70 B. A. Camley and F. L. H. Brown, *Phys. Rev. Lett.*, 2010, **105**, 148102.
- 71 D. P. Arnold, A. Gubbala and S. C. Takatori, *Phys. Rev. Lett.*, 2023, **131**, 128402.
- 72 S. Yang, X. Miao, S. Arnold, B. Li, A. T. Ly, H. Wang, M. Wang, X. Guo, M. M. Pathak, W. Zhao, C. D. Cox and Z. Shi, *Nat. Commun.*, 2022, **13**, 7467.
- 73 B. A. Camley and F. L. H. Brown, *Soft Matter*, 2013, **9**, 4767.
- 74 B. A. Camley and F. L. H. Brown, *J. Chem. Phys.*, 2014, **141**, 075103.
- 75 T.-S. Hsieh, V. A. Lopez, M. H. Black, A. Osinski, K. Pawłowski, D. R. Tomchick, J. Liou and V. S. Tagliabracchi, *Science*, 2021, **372**, 935–941.



- 76 S.-Z. Lin, R. Changede, A. J. Farrugia, A. D. Bershadsky, M. P. Sheetz, J. Prost and J.-F. Rupprecht, *Phys. Rev. Lett.*, 2024, **132**, 188402.
- 77 N. Ramakrishnan, P. B. Sunil Kumar and R. Radhakrishnan, *Phys. Rep.*, 2014, **543**, 1–60.
- 78 A. Winter, Y. Liu, A. Ziepke, G. Dadunashvili and E. Frey, *Phys. Rev. E*, 2025, **111**, 044405.
- 79 J. C. Stachowiak, F. M. Brodsky and E. A. Miller, *Nat. Cell Biol.*, 2013, **15**, 1019–1027.
- 80 B. H. Falkenburger, J. B. Jensen, E. J. Dickson, B.-C. Suh and B. Hille, *J. Physiol.*, 2010, **588**, 3179–3185.
- 81 T. H. Tan, J. Liu, P. W. Miller, M. Tekant, J. Dunkel and N. Fakhri, *Nat. Phys.*, 2020, **16**, 657–662.
- 82 M. C. Wigbers, T. H. Tan, F. Brauns, J. Liu, S. Z. Swartz, E. Frey and N. Fakhri, *Nat. Phys.*, 2021, **17**, 578–584.
- 83 L. B. Case, J. A. Ditlev and M. K. Rosen, *Annu. Rev. Biophys.*, 2019, **48**, 465–494.
- 84 J. M. Keegstra, F. Avgidis, Y. Mullah, J. S. Parkinson and T. S. Shimizu, *bioRxiv*, 2022, preprint, DOI: [10.1101/2022.12.04.518992](https://doi.org/10.1101/2022.12.04.518992).
- 85 D. Hathcock, Q. Yu and Y. Tu, *Nat. Commun.*, 2024, **15**, 8892.

